Discover Applied Sciences

Research

Silver doped anatase nanocomposite: a novel photocatalyst with advanced activity under visible light for waste-water treatment

Sherif Elbasuney[1] · Ahmed M. El-Khawaga[2] · Mohamed A. Elsayed[3] · Miguel A. Correa-Duarte[4]

Received: 20 September 2023 / Accepted: 11 March 2024
Published online: 23 March 2024

Abstract
Anatase is a universal semiconductor photocatalyst; however, its wide band-gap energy limits its entire solar spectrum absorption to only 5%. Anatase could be activated in the visible region via nobel metal deposition. This study reports on the facile synthesis of colloidal mono-dispersed anatase nanoparticles of 5 nm particle size via hydrothermal synthesis. Nobel metals (Silver, Nickel) were deposited on colloidal anatase surface. The photocatalytic activities of Ag–TiO_2, and Ni–TiO_2 were investigated for the degradation of basic fuchsin dye. Ag–TiO_2 nanocomposite demonstrated enhanced adsorption activity in dark, as well as superior photocatalytic. Ag–TiO_2 nanocomposite demonstrated enhanced removal efficiency by 70.8% under visible irradiation to virgin anatase. Ag–TiO_2 nanocomposite demonstrated enhanced oxygen-lattice with low binding energy using XPS analysis. Ag–TiO_2 experienced band gap energy of 2.35 eV compared with 3.2 eV for virgin anatase; this feature could secure enhanced solar absorption. Ag–TiO_2 demonstrated excellent photo-degradation efficiency of 88% with 0.3% H_2O_2 under visible light. Deposited silver could catalyze H_2O_2 decomposition and could promote free radical generation; Ag–TiO_2 nanocomposite is a promising photocatalyst for wastewater treatment applications.

Article Highlights

- Facile hydrothermal synthesis of anatase-based nanocomposites.
- Novel chemisorption and photocatalysis properties of anatase-based nanocomposites.
- Synergism between silver dopant TiO_2 and hydrogen peroxide.

Keywords Silver-doped anatase · Wastewater treatment · Visible irradiation · Basic fuchsin dye

✉ Sherif Elbasuney, sherif_basuney2000@yahoo.com; s.elbasuney@mtc.edu.eg; ✉ Ahmed M. El-Khawaga, Ahmed.Elkhawaga@gu.edu.eg; Ahmedelkhwaga15@gmail.com | [1]Nanotechnology Research Center, Military Technical College, Egyptian Armed Forces, Cairo, Egypt. [2]Department of Basic Medical Sciences, Faculty of Medicine, Galala University, New Galala City, Suez, Egypt. [3]School of Chemical engineering, Military Technical College, Egyptian Armed Forces, Cairo, Egypt. [4]Department of Physical Chemistry, Biomedical Research Center (CINBIO), Institute of Biomedical Research of Ourense-Pontevedra-Vigo (IBI), Universidad de Vigo, 36310 Vigo, Spain.

1 Introduction

One of the promising approaches to address the environmental and energy crises includes the efficient and affordable conversion of solar energy to chemical energy [1, 2]. Coinciding with this principle of sustainable chemistry; photocatalysis can secure a potential path toward solar energy conversion [3]. Photocatalysis can secure the opportunity to harness plentiful and clean solar energy through practical technology [4–6]. The landmark publication on photo-electrochemical technology sparked significant research interest in using semiconductor photocatalysts for wastewater treatment [4, 7–9]. However, the majority of investigated photocatalysts include wide band-gap semiconductors (such TiO_2 and ZnO); they expose photocatalytic activity when exposed to UV light. TiO_2 NPs are employed for degradation of organic contaminants [10, 11]. Moreover, TiO_2 is a potential semi-conducting materials for solar cell applications due to its high chemical stability, low toxicity [12, 13]. Furthermore, TiO_2 NPs are widely employed as photo-anode materials due to their high UV light absorption, good chemical solubility, superior corrosion resistance [14, 15]. Since UV light contributes to only 4% of the entire solar spectrum; this significantly hinders the practical use of wide band-gap semiconductors [16, 17].

Semiconductor photocatalysts can absorb photons with energies equal to or greater than their band-gap energy [18, 19]. The VB develops positive holes because of the photoexcitation of its electrons to the CB. Then the electron acceptors or electron donor species are reduced or oxidized at catalytic active spots on the semiconductor surface; consequently photocatalytic redox reactions could take place [20]. The photocatalytic reaction over semiconductor surface could be less effective due to the deactivation process of electron–hole pair re-combination. Therefore, the photocatalytic processes should speed up the separation and migration of the photogenerated electron–hole pairs to prevent their re-combination [21].

Recent advances in ZnO-based photocatalysts for water treatment technologies were reviewed by Lee et al. [22]. It was widely accepted that suitable architecture with a minimum amount of electron loss during the excitation stage and a maximum amount of photon absorption was necessary for the efficacy of ZnO photocatalyst in heterogeneous photocatalytic reactions [23].

Anatase offers a fresh starting point for the development of novel solar energy harvesting materials. The number of publications on photocatalysis has increased significantly since 2010, after the first report on TiO_2-based photocatalysts [24].

Nowadays, there has been an increase in research focused on the formation of new, effective photocatalysts. To extend the light absorption over the UV–Vis range, the combination of wide band-gap semiconductor photocatalysts with noble metals demonstrated promising features [25, 26]. The main role of transition metals is to act as dopant in an attempt to enhance the efficiency of electron–hole pair separation, and to extend the lifetime of charge carriers [27, 28]. Silver has attracted considerable attention as silver particles could act as electron trap that could prevent photo-generated charge carrier re-combination and could facilitating electron excitation via created local electrical field [29]. Nobel metals were found to be an efficient dopant in TiO_2 thin films [30].

Ground and surface water contamination by industrial dyes is a real threat to human health and living organisms. Synthetic dyes are widely used in textile and paper industry, leather manufacturing, plastics, cosmetics, rubber industries, and printing [31]. Basic Fuchsine (BF) dye is one of the most significant triphenylmethane dyes in textiles, ink, and leather industries. Its introduction into the environment is not only hazardous to aquatic life, but also carcinogenic to humans and animals [32]. Synthetic dyes removal from wastewater is an environmental challenge [2, 32, 33]. Thus, removal of BF is a great challenge for water purification and conservation [20].

In this work, titanium dioxide nanoparticles were developed via facile hydrothermal synthesis. Nobel metal deposition was conducted to develop high quality Ag–TiO_2 and Ni–TiO_2 nanocomposites. The developed heterogeneous photocatalysts were employed for wastewater treatment. Ag–TiO_2 nanocomposite demonstrated superior photocatalytic activity under ultraviolet, and visible region. This superior performance was attributed to the deposited Ag metal. The effect of solution pH, photocatalyst dosage, dye initial concentration, and H_2O_2 addition on the degradation efficiency was also investigated and optimized.

2 Materials and methods

2.1 Chemicals

Anatase nanoparticles (NPs) were developed via hydrothermal synthesis. The adopted titanium salt precursor was an aqueous solution 50 wt% of titanium IV bis (ammonium Lactato) di hydroxide (TIBALD). Hydrogen peroxide (H_2O_2, 30

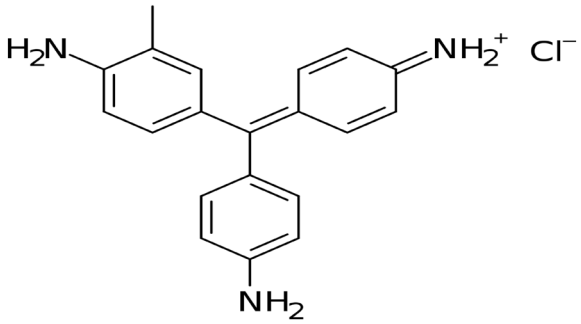

Fig. 1 The chemical structure of Basic Fuchsine dye

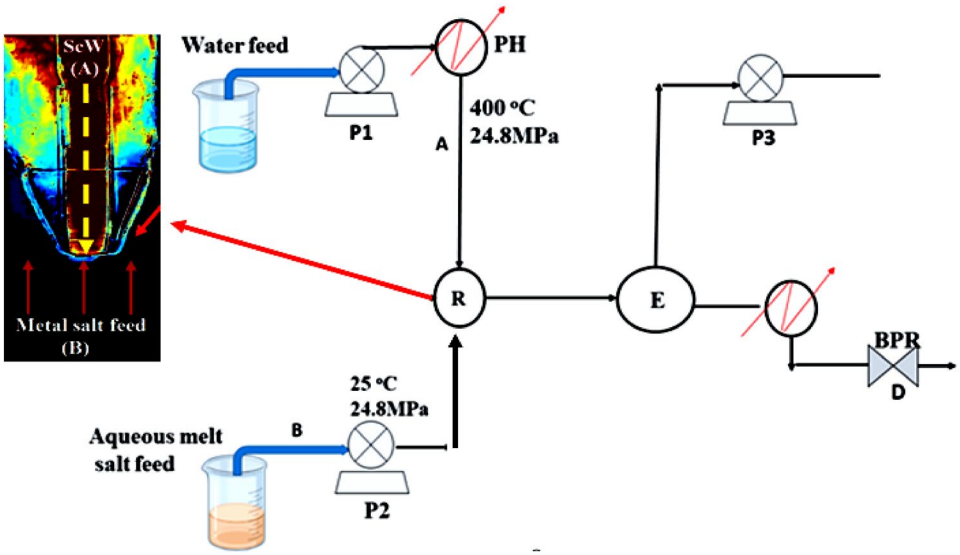

Fig. 2 Flow diagram of continuous hydrothermal synthesis system

vol%) was employed for OH^- ions during hydrothermal synthesis. Silver nitrate, and nickel nitrate (Aldrich, 99.99%) were employed as the precursor for nobel metal dopant. Basic Fuchsine (a fluorescent dye composed of rosaniline, magenta II, pararosaniline, and new fuchsine, Aldrich, < = 100%) was employed as a contaminant. The chemical structure of BF dye is represented in Fig. 1. All chemicals were used as perceived without further treatment.

2.2 Nanoparticle synthesis

2.2.1 Synthesis of anatase nanoparticles

Colloidal anatase (TiO_2) particles with consistent product quality were fabricated sustainably via established continuous hydrothermal processing (Fig. 2).

Where super-critical water (Flow A) at 225 bars and 415 ℃ (20 ml/min) was pumped down against an up flow of cold metal salt (Flow B) (0.05 M TIBALD) at 245 bars and 20 ℃ (10 ml/min.). NPs were formed at the border of the two fluids inside the counter reactor (C). The fabricated anatase NPs were cooled down before collection point (E).

2.2.2 Synthesis of anatase-based nanocomposite

The synthesized colloidal anatase (TiO_2) nanoparticles were collected from the medium in which they were produced and then dispersed again in noble metal nitrate solution (silver, nickel) using an ultrasonic bath for 1 h. The weight percentage of noble metal ions (Ag^+, Ni^+) to anatase was 1:9. Sodium borohydride was employed as a reducing agent. The stoichiometric ratio of sodium borohydride to noble metal ions (Ag^+, Ni^+) was 3:1. The reduction of noble metal was conducted under vigorous magnetic stirring for 30 min, to ensure optimal homogeneity and even deposition of the noble metal on TiO_2 surface.

2.3 Nanoparticle characterization

The morphology and elemental mapping of synthesized Ag–TiO_2, and Ni–TiO_2 were determined by SEM (JWEL JSM 6010 LA, Japan) equipped with EDAX detector (X-act, Oxford instruments). The crystalline structure of TiO_2, Ag–TiO_2, Ni–TiO_2 were assessed using XRD; the diffraction pattern was collected using a Siemens D-5000 powder X-ray diffractometer. The chemical bonding and elemental analysis of Ag–TiO_2 and Ni–TiO_2 nanocomposites were determined by X-ray photoelectron spectroscopy (XPS) Thermo Scientific K-Alpha ESCA instrument.

2.4 Photocatalytic degradation of basic fuchsine (BF)

TiO_2, Ag–TiO_2, and Ni–TiO_2 NPs (10 mg) were mixed with 50 ml of BF solution in separate 125 ml beakers with initial concentration $C_0 = 20$ ppm, 25 ℃ for 90 min in the dark, until adsorption–desorption equilibrium was reached. The activity of anatase-based nanocomposites was measured for the degradation of BF under both UV and visible light irradiation in separate experiments. The used UV reactor was cylindrical shape having dimensions of 27 cm length, 2.5 cm diameter. The source of UV light is a 10 W high pressure mercury lamp (wavelength 254 nm). On the other hand, the photo-reactor was irradiated by a visible lamp composed of 52 white light LEDs (nominal power: 55 W) with wavelength emission in the range 400–800 nm surrounded by aluminum reflectors to minimize irradiation loss. The lamp was positioned at the top; the distance between the light source and the reactor was 10 cm. A sample of the BF suspension (1 ml) has been collected using a syringe fitted with a filter (2.5 mm pore size) at regular time intervals of irradiation. The degradation rate of BF was determined by analyzing the changes in BF concentration over time using UV–Vis spectrophotometer (Agilent Technologies Cary 60 UV–Vis), at maximum absorption wavelength (λ max) of 546 nm. Deionized water was utilized as a reference solution [34].

3 Results and discussions

3.1 Characterization of nanoparticles

The fabricated anatase (TiO_2) NPs demonstrated mono-dispersed particles of 5 nm average particle size. TEM micrographs demonstrated high-quality particles with uniform particle sizes as illustrated in Fig. 3.

XRD pattern confirmed high-quality anatase crystalline structure. Sharp and intense peaks were observed at $2\Theta = 25.281°$ (101), 37.801° (004), 48.050° (200), 55.062° (211), and 62.690° (204). XRD peaks were found to be identical with ICCD card no. 00–021-1272 [35]. Ag–TiO_2 experienced intense characteristic peaks of silver at $2\Theta = 38.117°$, 44.279°, 64.428°, and 77.475° corresponding to (111), (200), (220), and (311) respectively. Silver peaks were found to be in good accordance with ICCD card no. 00–004-0783. It can be assumed that silver NPs were effectively deposited on the surface of TiO_2 NPs (Fig. 4a). The XRD pattern of Ni–TiO_2 was investigated to virgin TiO_2. XRD diffractogram of Ni–TiO_2 demonstrated XRD diffractogram similar to TiO_2. Even though deposited nickel demonstrated a complete change of TiO_2 from white to yellowish green. The main nickel signals at $2\Theta = 44.508$, 51.8472, and 76.372, corresponding to (111), (200), (220), and (311) respectively, were not observed; this can be ascribed to the low XRD signature of nickel to that of TiO_2 (Fig. 4b).

The dispersion and quantification of deposited nobel metal particles were investigated using SEM. EDAX micrographs of Ag–TiO_2 nanocomposite demonstrated uniform deposition of silver metal (Fig. 5a). Ni–TiO_2 nanocomposite demonstrated uniform dispersion of nickel particles on the surface of TiO_2 particles (Fig. 5b).

The quantification of deposited nobel metals was evaluated via EDAX detector. While Ag–TiO_2 nanocomposite demonstrated silver content of 2.33 at% (Fig. 6a); Ni–TiO_2 nanocomposite demonstrated nickel content of 2.59 at% (Fig. 6b).

Elemental analysis as well as binding energy was investigated using XPS analysis. Precise elemental binding energies (BE) were determined to carbon C1s peak at 284.8 eV. XPS spectroscopy was employed to identify and quantify the elements in the sample. Deposited nobel metals nickel and silver were identified via the binding energy of Ni2P and Ag3D respectively (Fig. 7).

Survey spectra offered the determination of the elemental composition of Ag–TiO_2, and Ni–TiO_2 nanocomposite (Table 1).

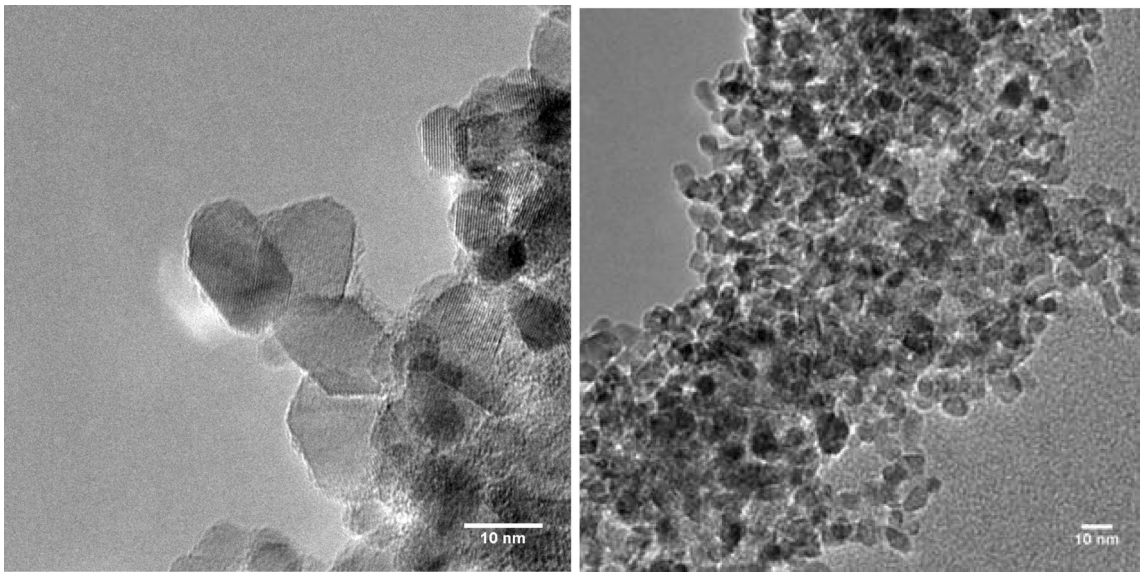

Fig. 3 TEM micrographs of synthesized anatase (TiO_2) nanoparticles

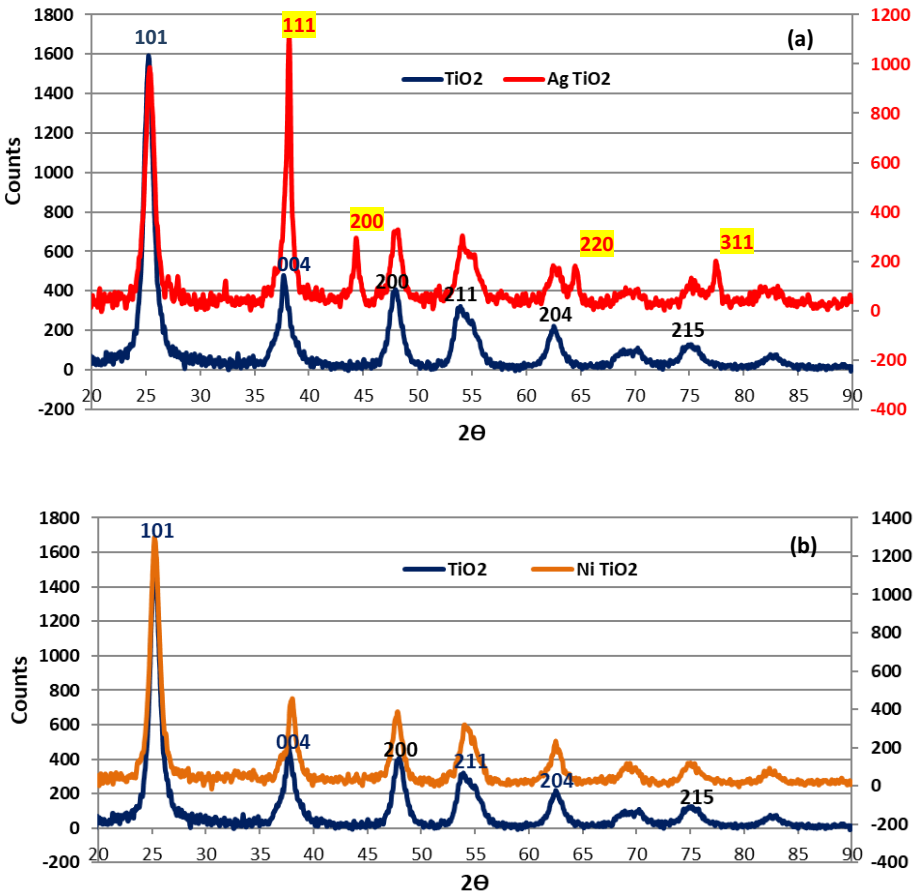

Fig. 4 XRD diffractogram of Ag–TiO_2 (**a**), Ni–TiO_2 (**b**) nanocomposite to virgin TiO_2

Ag–TiO_2 sample demonstrated a similar value of O/Ti to virgin TiO_2; this indicates that the deposited silver is in the metallic form. The analysis of the oxidation state of silver relies on the position of auger lines which makes it possible to determine the chemical environment of silver. Values of Auger parameter allow us to determine the chemical environment of silver [36, 37]. The auger parameter of Ag–TiO_2 demonstrated value of 726.03 which corresponds to Ag (0) (Fig. 8).

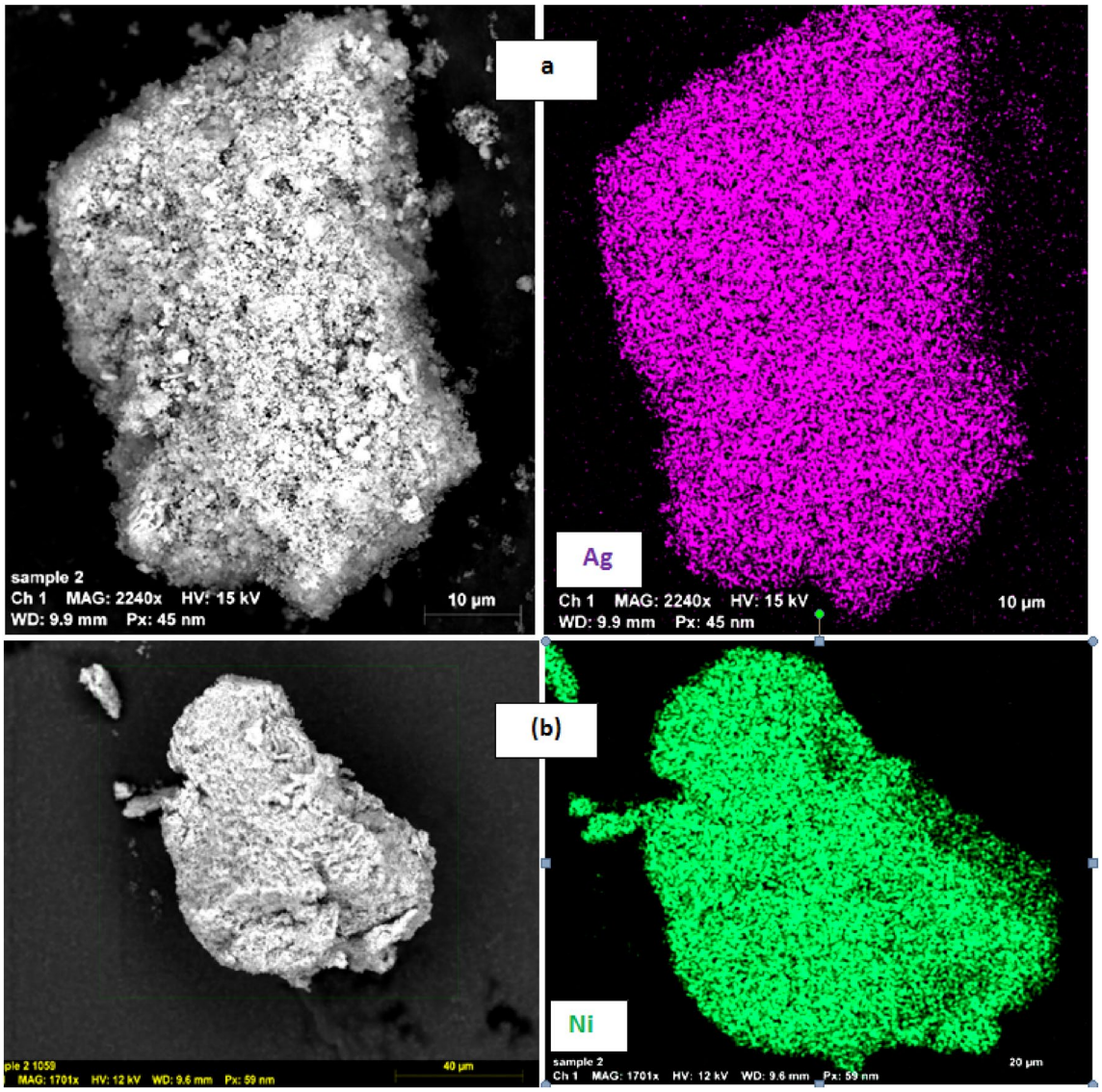

Fig. 5 Elemental mapping of Ag–TiO_2 (**a**), Ni–TiO_2 (**b**) nanocomposite

The values of Ag3d binding energy as well as Auger Parameter value are tabulated in Table 2.

Auger parameter confirmed XPS survey spectra and O/Ti ratio. Auger parameter confirmed the successful deposition of the silver element on the surface of TiO_2. Ni–TiO_2 nanocomposite experienced an increase in O/Ti ratio; the deposited nickel could be partially in the form of oxide or hydroxide. This feature was further investigated via the binding energy of Ni2P (Fig. 9).

Ni2P3/2 demonstrated three peaks fitting correspond to nickel hydroxide. The binding energy of Ni2P3/2 of the center of gravity for Ni2P3/2 demonstrated 856.57 eV; this value is slightly higher than that corresponding to Ni $(OH)_2$ compound of 855.8 eV. It can be concluded that the deposited nickel is a hybrid of nickel and nickel hydroxide [38].

The impact of deposited noble metal on lattice oxygen binding energy was investigated via O1S scan. O1S binding energy of Ni–TiO_2, and Ag–TiO_2 was investigated to virgin TiO_2. Whereas virgin TiO_2 demonstrated O1S binding energies corresponding to oxide lattice (A), O–H surface (B), and organic hydrocarbon (C). Deposited nickel was found to increase the atomic percent of both O1S (B), and O1S (C); this can be ascribed to the fact that the deposited nickel is a combination of Ni, and $Ni(OH)_2$. On the other hand, the deposited silver was found to eliminate O1S (C) of high binding energy and increase the O1S (A) and O1S (B). This indicates that the deposited silver is in zero valence state Ag(0) [39]. The Quantification of O1S binding energies and relative percentages are tabulated in Table 3.

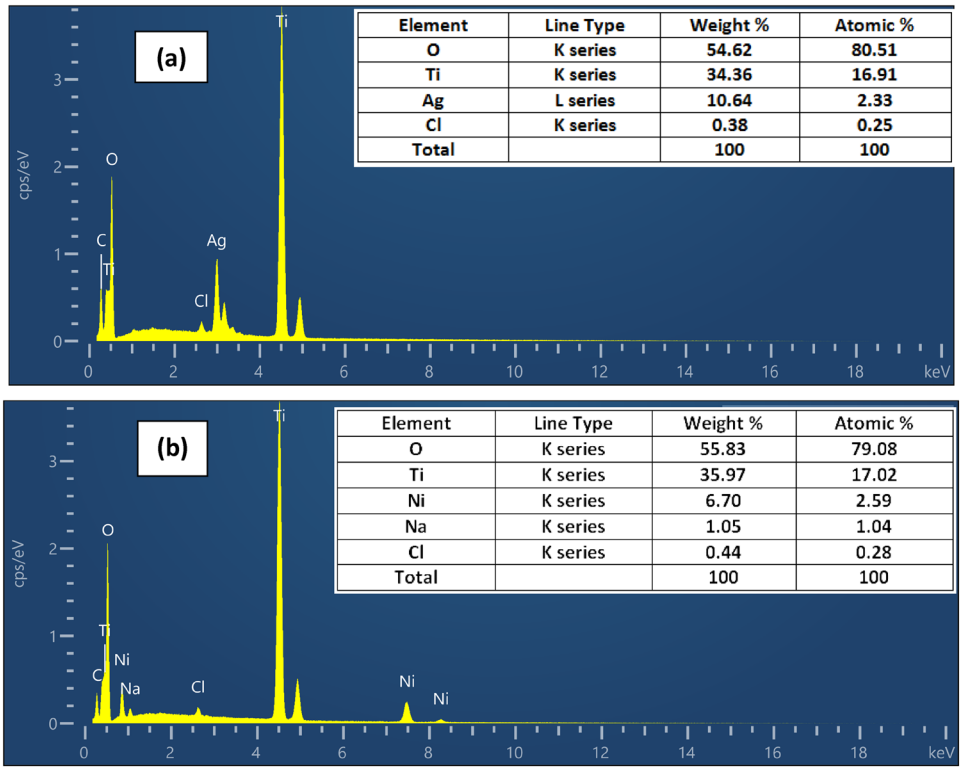

Element	Line Type	Weight %	Atomic %
O	K series	54.62	80.51
Ti	K series	34.36	16.91
Ag	L series	10.64	2.33
Cl	K series	0.38	0.25
Total		100	100

Element	Line Type	Weight %	Atomic %
O	K series	55.83	79.08
Ti	K series	35.97	17.02
Ni	K series	6.70	2.59
Na	K series	1.05	1.04
Cl	K series	0.44	0.28
Total		100	100

Fig. 6 Elemental composition of Ag–TiO_2 nanocomposite (**a**), Ni–TiO_2 nanocomposite (**b**)

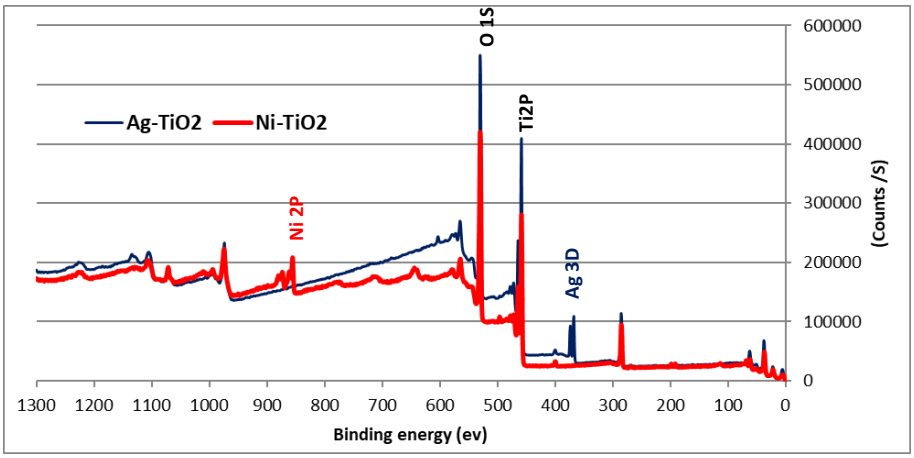

Fig. 7 XPS survey spectra of Ag–TiO_2, Ni–TiO_2 nanocomposite

Table 1 Elemental composition of Ag–TiO_2, and Ni–TiO_2 nanocomposites

XPS Elemental atomic percent (At%)								
Sample	C	O	Ti	Ni	Ag	N	Cl	O/Ti
TiO_2	41.97	40.18	14.74	–	–	1.86	1.25	2.73
Ni–TiO_2	27.41	49.47	14.23	5.01	–	2.21	1.67	3.48
Ag–TiO_2	29.33	47.7	17.88	–	2.06	2.16	0.79	2.67

It is obvious that the deposited Ag (0) eliminated O1S (C) of high binding energy; in the meantime, it offered high percentages of low binding energy O1S. This can offer novel catalyzing ability. The spectra of O1S scan for investigated samples are represented in Fig. 10.

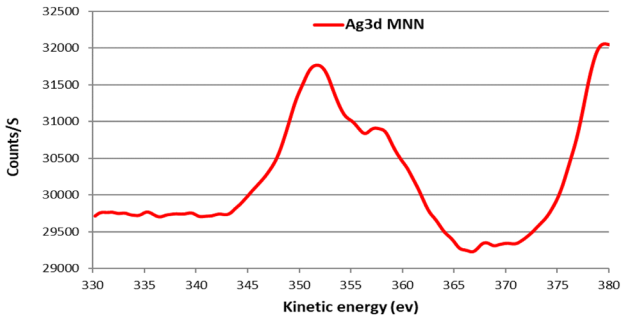

Fig. 8 Auger parameter for Ag element in Ag–TiO_2 nanocomposite

Table 2 Silver Ag3d binding energy and Auger Parameter

Silver (Ag3d) Binding energy BE (ev)/Relative percent (Rel%)				
Sample	Ag3d5/2 oxidized	Ag3d5/2 Ag(0)	AgM4N45N45/Auger Peak	Auger parameter Ag3d5(BE) + Auger (KE)
Ag–TiO_2	–	367.58/100%	358.45	726.03

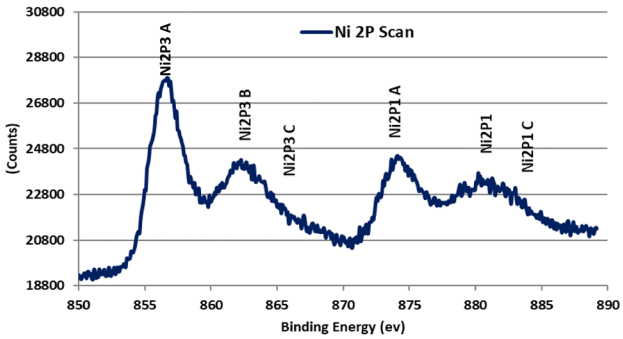

Fig. 9 The binding energy of Ni2P of Ni–TiO_2 nanocomposite

Table 3 O1S Binding energies and at% of TiO_2, Ni–TiO_2, and Ag–TiO_2

Oxygen (O1s) Binding Energy (BE)/Relative Percent (Rel. %)			
Sample	O1 S (A) Oxide/lattice	O1 S (B) O–H	O1 S (C) (C) Organic
TiO_2	529.75/77.73%	531.29/15.4%	532.66/6.87%
Ni–TiO_2	529.76/18.38%	530.9/58.69%	532.79/22.93%
Ag–TiO_2	529.73/76.13%	531.13/23.87%	–

It is obvious that silver particles eliminated the hydrocarbon oxygen of high binding energy and offered an increase in lattice and hydroxyl oxygen of low binding energy. This could offer novel photocatalytic properties. These findings could demonstrate the surge of O/Ti value for Ni–TiO_2 sample.

3.2 Analysis of optical properties

The analysis of diffuse reflectance was performed using a Perkin Elmer UV–visible spectrophotometer to determine the absorption peaks and bandgap energies of the Ni–TiO_2 and Ag–TiO_2 nanoparticles. The absorption and reflectance maxima of surface plasmons were acquired and depicted in Fig. 11. The findings indicate that the optical characteristics of the specimens vary depending on the type of doping. The observed phenomenon can be attributed to the plasmon resonance effect exhibited by Ag–TiO_2 and Ni–TiO_2 nanoparticles [40–42]. These nanoparticles possess a collective oscillation of their outermost electrons and can absorb visible light [43]. To assess the optical band-gap energy of the Ag–TiO_2 and Ni–TiO_2 NPs samples, the Kubelka–Munk algorithm, $F(R) = (1 - R)^2/2R$, was utilized [44]. Where R stands for reflectance

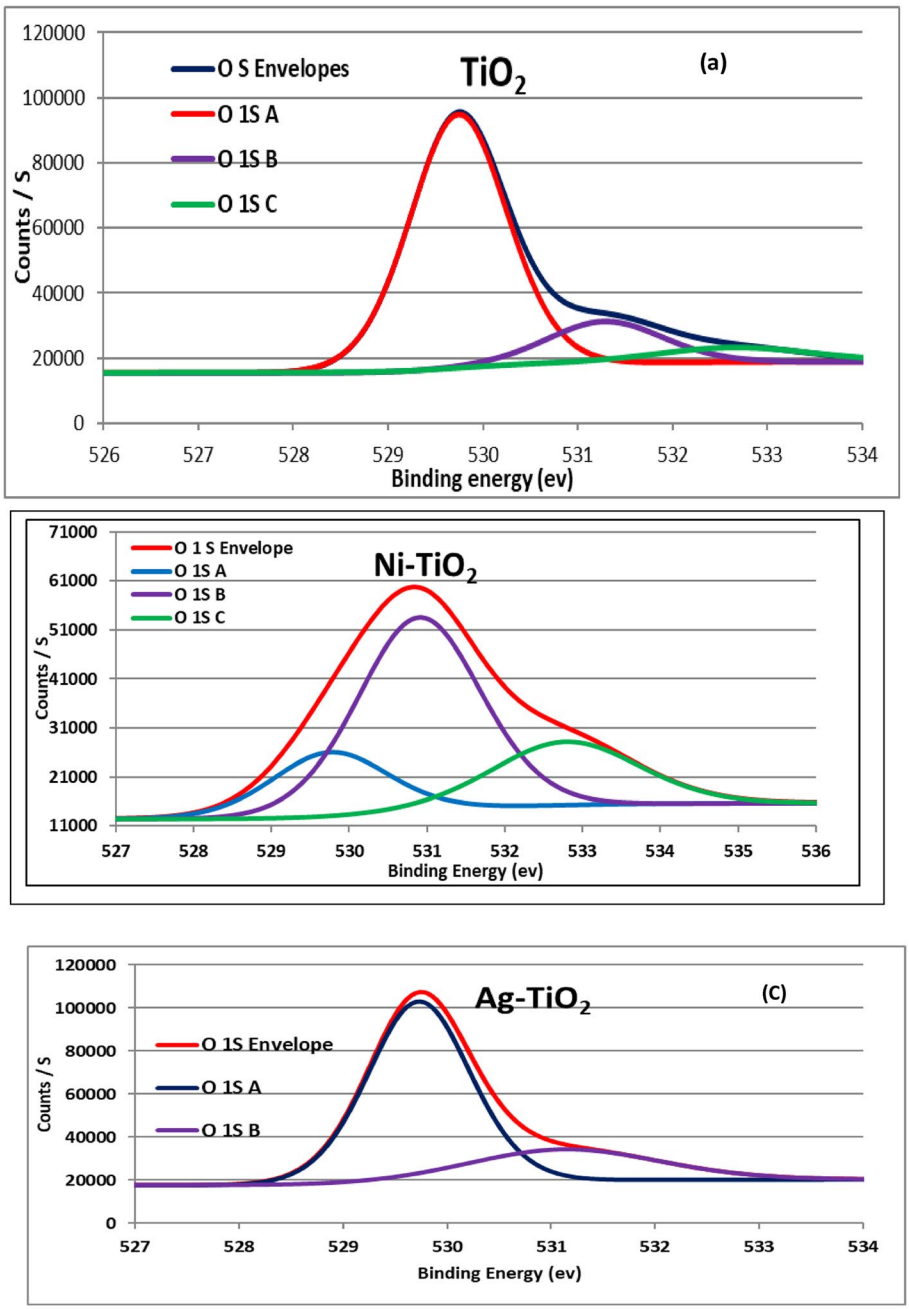

Fig. 10 O1S spectra for: anatase TiO_2 (**a**), Ni–TiO_2 (**b**) Ag–TiO_2 (**C**)

and F(R) represents the amount of absorption. The optical band gap energy for the Ag–TiO_2 and Ni–TiO_2 NPs are tabulated in Table 4 and represented in Fig. 11. It is obvious that anatase based nanocomposite samples demonstrated two band gaps, due to the existence of two phases [44]. This finding was found to be in good accordance with XRD data; furthermore, the synergistic effect between TiO_2 and noble metals (Ag and Ni) could decrease the band gap energy.

3.3 Removal performance of Ag–TiO_2 and Ni–TiO_2 NPs toward (BF) dye

The removal of BF was measured at $\lambda_{max} = 546$ nm and the calibration curve of BF was done using serial dilution (2.5, 5, 10, 15, and 20 ppm) of BF as demonstrated in Fig. 12 [45].

This material possesses the potential to act as a carcinogen and has the capacity to induce irritation, dermatitis, and conjunctivitis. The act of consuming a substance has the potential to induce irritation in the gastrointestinal tract, leading to symptoms such as nausea, vomiting, and diarrhea [46–48]. Therefore, BF was chosen as a model contaminant to

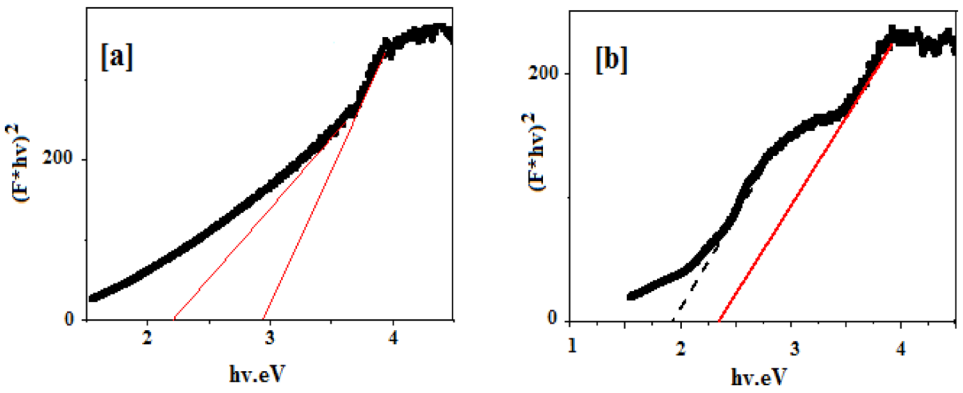

Fig. 11 Kubelka–Munk plots of samples displaying the bandgap energies of **a** Ni–TiO_2, and **b** Ag–TiO_2

Table 4 The optical band gap energies

Eg, eV	1	2
Ni–TiO_2	2.20	2.95
Ag–TiO_2	1.93	2.35

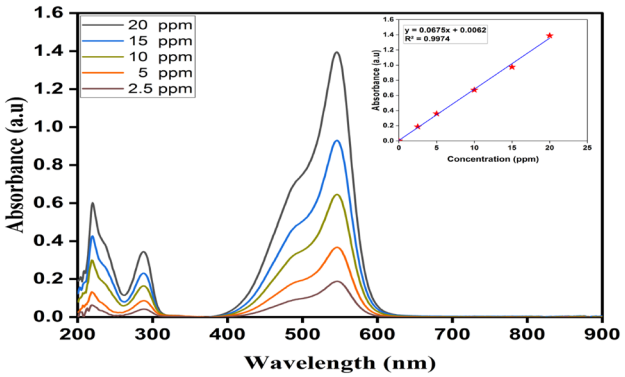

Fig. 12 UV–Vis. A spectrum of Basic fuchsine (BF) and calibration curve at different concentrations of BF

evaluate the photocatalytic activity of the synthesized photocatalysts. Comparative investigation for different dye removal aspects including adsorption, photocatalysis using UV irradiation, and photocatalysis using visible light irradiation were evaluated for Ag–TiO_2 and Ni–TiO_2 to virgin TiO_2.

While virgin anatase demonstrated only 10% removal via adsorption after 90 min in dark; Ag–TiO_2 and Ni–TiO_2 experienced removal efficiency of 20.2 and 15.9% respectively (Fig. 13a). Photocatalytic removal activity of virgin anatase under UV irradiation was limited to 43.2% after 90 min. Ag–TiO_2 and Ni–TiO_2 experienced removal efficiency of 54.3, and 46.8% respectively (Fig. 13b). The superior dye removal efficiency was achieved via Ag–TiO_2 under visible light irradiation. Ag–TiO_2 experienced dye removal of 66.8%, compared with 39.1 and 59% for virgin anatase, and Ni–TiO_2 respectively as demonstrated in (Fig. 13c).

3.4 Synergistic catalytic effect of Ag–TiO_2 and Ni–TiO_2 under UV and visible light

Following the process of adsorption, ultraviolet (UV) light was applied to the BF removal system, which included the addition of Ag–TiO_2 and Ni–TiO_2 as photocatalysts. The efficacy of BF removal was enhanced by up to 54.3% after 90 min when Ag–TiO_2 and Ni–TiO_2 were introduced into the BF solution and subjected to UV light irradiation. The analysis of the light absorption results under dark and light irradiation conditions revealed that the primary mechanism responsible for the elimination of BF was the photocatalytic degradation facilitated by the Ag–TiO_2 and Ni–TiO_2 nanocomposite. The maximum removal effectiveness of 54.3% was observed after a duration of 90 min. This can be attributed to the higher photon energy present in UV light and the impact of the metal–semiconductor hetero-junction created within the nanocomposite. The presence of this hetero-junction facilitates the effective separation of charges and amplifies the absorption of incident light [49].

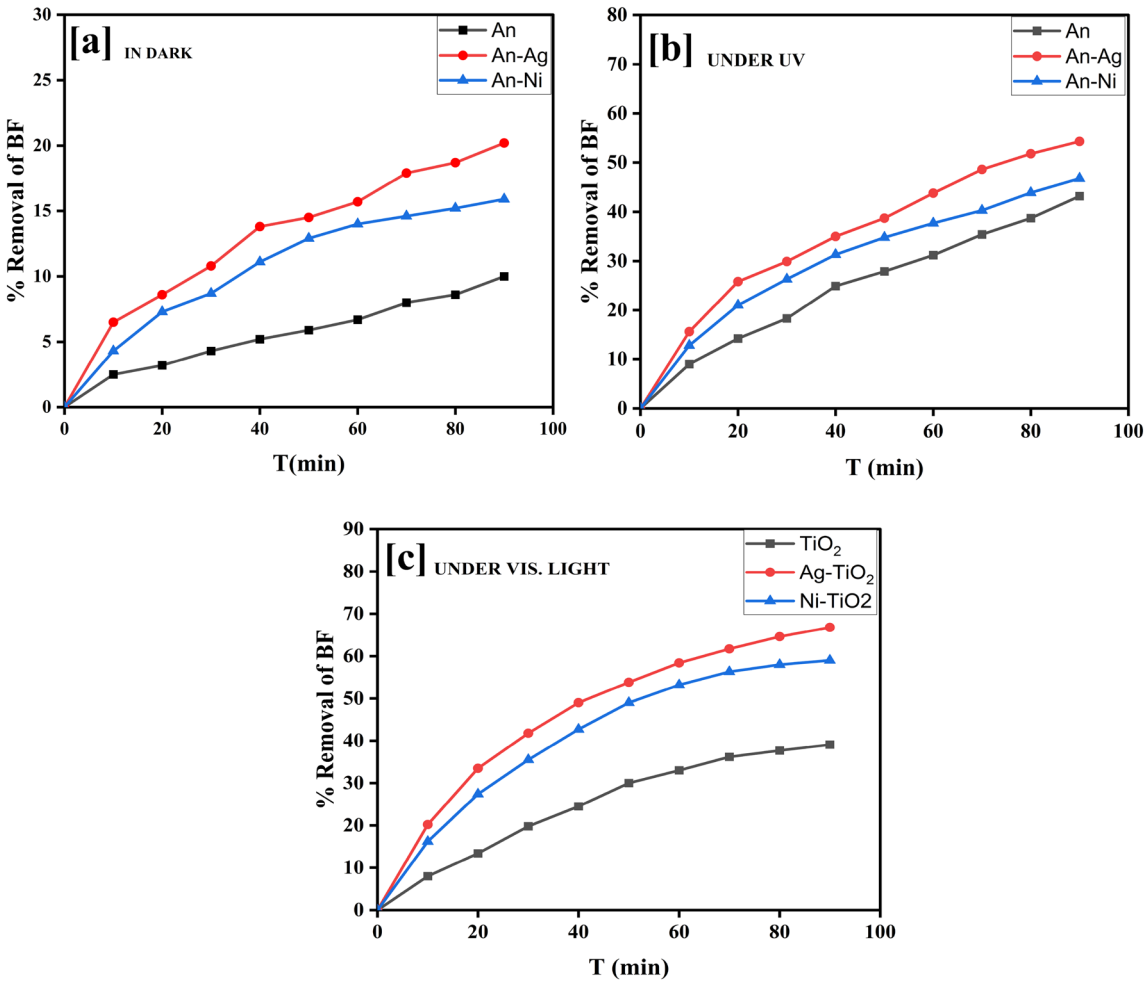

Fig. 13 % Removal of BF within 90 min by virgin TiO_2, Ag–TiO_2 and Ni–TiO_2, due to: **a** Adsorption activity in dark, **b** Photocatalysis under UV, and **c** Photocatalysis under Visible light

From Fig. 13C, it is observed that Ag–TiO_2 and Ni–TiO_2 photocatalysts showed a unique photocatalytic activity against BF compared to virgin TiO_2. Whereas Ag–TiO_2 and Ni–TiO_2 experienced BF removal by 66.8 and 59.0% respectively; virgin anatase demonstrated BF removal by 39.1% in 90 min under Visible light irradiation. The doping of Ag to anatase promises to generate several effects on its photocatalytic activity through the following methods. The incorporation of metal nanoparticles in photocatalysts has the potential to provide several beneficial effects. Firstly, the presence of metal nanoparticles can facilitate the separation of electrons and holes by serving as electron traps. Secondly, the introduction of metal nanoparticles can extend the absorption of light to the visible range, thereby enhancing the excitation of surface electrons through Plasmon resonances induced by visible light. Lastly, the inclusion of metal nanoparticles can bring about modifications to the surface characteristics of photocatalysts [50, 51].

It is widely accepted that the increase in photocatalytic activity by Ag dopant could be ascribed to the increase in interfacial charge transfer efficiency for TiO_2, as well as enhanced charge pair separation and thereby inhibiting their recombination [52]. The photocatalytic activity by Ag–TiO_2 is explained below in the mechanism section.

3.4.1 Effect of pH value on removal of BF

The pH of the solution is a crucial factor in removal studies. The impact of initial pH values of the BF solution was investigated under specific experimental conditions, including the use of 10 mg of the prepared nanocomposite, 50 ml of a 10 ppm BF solution, and a temperature of 25 °C. Figure 14a displays a graph illustrating the change in BF removal (%) over time at various solution pH levels ranging from 3.0 to 9.0. It was observed that the highest level of BF removal at equilibrium occurred at pH 9.0.

In order to calculate the point of zero charges (PZC) of the Ag–TiO_2 nanoparticles (NPs), a quantity of 0.01 g of the Ag–TiO_2 NPs was mixed into a 50 mL solution of 0.01 M NaCl [53, 54]. The pH values of the solutions were modified using hydrochloric acid (HCl) or sodium hydroxide (NaOH) to achieve pH levels of 2, 4, 6, 8, 10, and 12. The samples were subjected to agitation at a speed of 200 revolutions per minute (rpm) for 48 h. The pH values of the solutions were determined after the separation of (Ag–TiO_2 nanoparticles). The determination of the pH at the point of zero charge (PZC) was accomplished via a graph illustrating the relationship between the final pH and the initial pH. Based on the data presented in Fig. 14b, it can be observed that the (PZC) corresponds to the pH value at which there is negligible difference between the final and initially measured pH values. The PZC was found to be at pH 6.75. This means that the surface charge of the photocatalyst, specifically the Ag–TiO_2 nanoparticles, exhibits positive charge when the pH is below the PZC, and negative charge when the pH is above the PZC. Moreover, in cases where the pH of the solution equals the pH of the PZC, the surface charge of the photocatalyst becomes neutral, resulting in a low electrostatic force between the photocatalyst surface and ions (specifically BF ions) [55–57]. This result explained the reason for the observed maximal photocatalytic degradation of BF at pH 9.0, as depicted in Fig. 14a. Therefore, it can be concluded that the net surface charge of the Ag–TiO_2 nanoparticles is negative, resulting in an attraction towards the positive charge of BF. This interaction ultimately enhances the photocatalytic degradation of BF [58]. The degradation of BF during photocatalysis demonstrated decrease as the pH reached 5.0. This phenomenon can be attributed to the positive net surface charge of the Ag–TiO_2 nanoparticles, which leads to repulsion forces between the positive charge of BF and the positive net surface charge of the Ag–TiO_2 nanocomposite. This positive net surface charge is observed at pH levels below 6.2.

In general, the solution pH significantly impacted the photocatalytic degradation rate of pollutants. Anatase, under UV light irradiation, generates electron–hole pairs. Holes react with water to produce hydroxyl radicals ($OH^{\bullet}$), powerful oxidants that degrade pollutants. At acidic pH (pH < 7), protonation of surface hydroxyl groups (TiOH) to create $TiOH_2^+$, could enhance hole capture and OH• generation. Increased OH• radicals could lead to fast degradation rates at optimal pH. At basic pH (pH > 7), De-protonation of TiOH to TiO^- could reduce hole capture and OH• generation. Low OH• could result in slow degradation rates. Overall: Anatase TiO_2 exhibits a bell-shaped curve for degradation rate constants with respect to pH, peaking at an optimal pH (usually around 3–5). Silver dopant could introduce additional energy levels within the band gap of TiO_2. This could facilitate visible light absorption and charge separation and could boost photocatalytic activity [59]. Silver dopant demonstrated shift in the optimal pH range for maximum degradation rate compared to un-doped TiO_2. The shift depends on the doping level, silver distribution, and the target pollutant [60]. Doping might influence surface properties and adsorption behavior of pollutants, affecting the pH dependence. The influence of pH on silver-doped TiO_2 can be much complex due to the interplay of various factors [61].

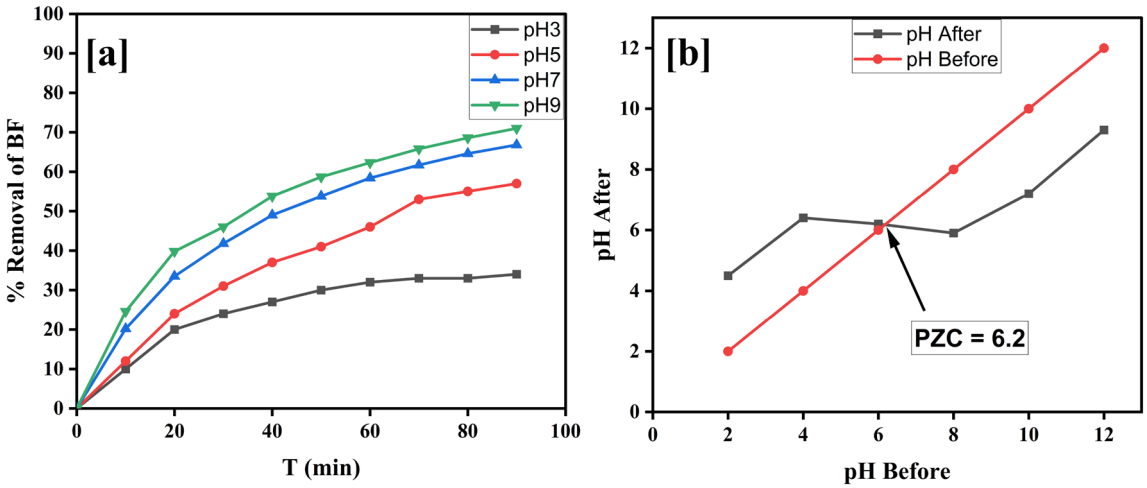

Fig. 14 Showing **a** (%) removal of BF at different pH values (3.0, 5.0, 7.0 and 9.0), 50 ml Ag–TiO_2 (10 mg), initial concentration of BF (10 ppm) at 25 ℃. **b** Point of zero charge (PZC) of Ag–TiO_2

3.4.2 Effect of initial concentration of BF and amount of Ag–TiO_2 nanocomposite

The impact of ionic strength on the removal process was investigated by varying the starting concentration of BF while maintaining all other reaction conditions constant. Figure 15a demonstrates the relationship between the percentage of elimination and the contact time for various initial BF concentrations (5.0, 10.0, and 15.0 ppm).

The results indicate that the efficiency of degradation has an inverse relationship with the concentration of BF. Particularly, the produced nanocomposite demonstrates the capability of effectively degrading BF, even when present at high initial concentrations, under visible light irradiation.

The impact of different nanocomposite doses on the removal efficacy of BF under visible light was assessed. The amount of the photocatalyst used was varied at 5, 10, and 20 mg, while maintaining a constant concentration of BF at 10 ppm, as depicted in Fig. 15b. The findings of the study demonstrated a positive correlation between the dosage of the photocatalyst (ranging from 5 to 20 mg) and the efficiency of pollutant removal. The observed correlation between the increase in removal efficiency and the amount of photocatalyst could be attributed to the increase in the available active area or active sites of the photocatalyst to volume ratio of the BF solution [18, 62]. TiO_2@Ag_3 composite exhibited superior photocatalytic performance with removal efficiency of 97% compared with 77% for TiO_2 against Rhodamine B dye [63]. Doping with Ag was beneficial to provide efficient separation of the photogenerated electron–hole and interface charge transfer [64].

The dependence of photo-catalytic degradation reaction rate constants on the catalyst dose can differ significantly between pristine anatase and its silver-doped counterpart. Pristine anatase demonstrated an increase in the reaction rate with increase in catalyst doze; this can be ascribed to the larger number of available active sites on the catalyst surface [65]. However further increases in TiO_2 dose can lead to a decrease in reaction rate constants; this can be attributed to several factors such as light shielding, excess catalyst particles can block light from reaching the active sites within the reaction mixture, hindering photoexcitation and radical generation [66]. Increase in catalyst concentration could promote particle aggregation, reducing their effective surface area and accessibility to reactants. High catalyst density can facilitate recombination of photogenerated electron–hole pairs, thereby reducing the efficiency of charge separation and radical formation [67].

Silver-doped TiO_2 demonstrated enhanced visible light absorption: silver dopant could introduce new energy levels within TiO_2 bandgap, allowing it to absorb visible light, potentially leading to higher reaction rates under broad light spectra [68]. Plasmonic effect, depending on the specific silver distribution and morphology, plasmonic resonance can enhance the local electric field at the catalyst surface, potentially promoting charge separation and improving photocatalytic activity [69]. Generally, the optimal catalyst dose for Silver-doped TiO_2 might be lower compared to pristine TiO_2 due to potential light-shielding and deactivation concerns [70].

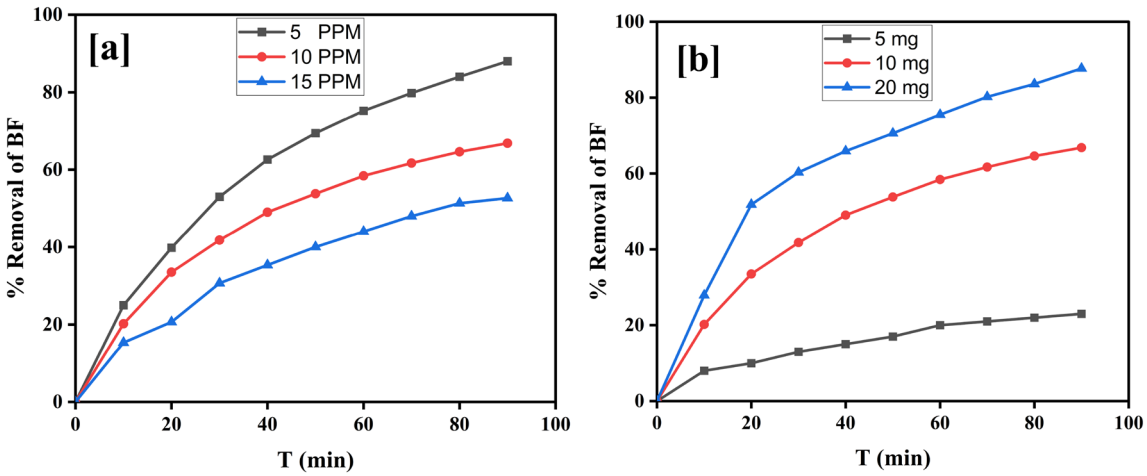

Fig. 15 Effect of initial concentration of BF (5, 10, 15) ppm (**a**), and photocatalyst dose on the removal efficiency of BF (50 ml BF solution (10 ppm) (**b**), Temp. = 25 ℃ and pH 9)

3.4.3 Kinetic studies

The degradation rate of BF can be calculated using the following equation:

$$-\ln C_t/C_0 = -Kt \quad (1)$$

where C_t and C_0 are the remaining and the initial concentrations (ppm) of BF respectively, while t is the removal time (min) and k represents the removal rate constant (min^{-1}) [33, 71–73]. Figure 16a. shows a relation of $-\ln C_t/C_0$ vs. t.

The results indicated that the kinetics of the removal reaction followed rate laws that can be approximated as pseudo-first order. Furthermore, as seen in Fig. 16b, it can be observed that an elevation in BF concentration results in a reduction of the apparent pseudo-first-order rate constants. The dependence of reaction rate constants on the concentration of BF is consistent with the findings reported in the existing literature [58, 74]. The relationship between the concentration of Basic Fuchsin (BF) and the photocatalytic degradation rate constant (k) is complex and can vary depending on several factors [75]. However, some general trends have been observed. As the BF concentration increases, the number of dye molecules available for interaction with the photocatalyst increases, leading to a rise in the reaction rate, and rate constant [76]. At a certain point, the available catalyst surface area becomes saturated with dye molecules, and further increase in BF concentration might not significantly affect the rate constant. However, when the BF concentration is very high, it could act as an inner filter and could impede incident light from reaching the catalyst surface. This could reduce the efficiency of photo-excitation and electron transfer, with a decrease in the degradation rate [77].

3.5 Synergistic catalytic effect of Ag–TiO_2 nanocomposite with H_2O_2

The addition of H_2O_2 resulted in an enhanced photocatalytic performance of the Ag–TiO_2 nanocomposite. The primary cause of this phenomenon could be correlated to the superior electron-accepting characteristics of H_2O_2 in comparison to molecular oxygen. This property has the potential to accelerate the rate of photocatalysis by mitigating the adverse effects of electron–hole recombination and facilitating the formation of active hydroxyl radicals [78]. It may be suggested that the observed improvement in the photodegradation of BF is attributed to the combined action of H_2O_2 and the synthesized photocatalysts, as depicted in Fig. 17.

3.6 Mechanism of photocatalytic activity of Ag–TiO_2 nanocomposite

Anatase is the most widely employed photocatalyst; however, its limitation is related to large ban-gap energy that limit its performance to ultraviolet (UV) light rather than visible light. This feature could restrict its practical use under visible light conditions [79]. To overcome this limitation, we have explored doping strategies, including incorporating silver (Ag) into the anatase structure. Silver dopant modified the electronic band structure of anatase TiO_2, extended its absorption

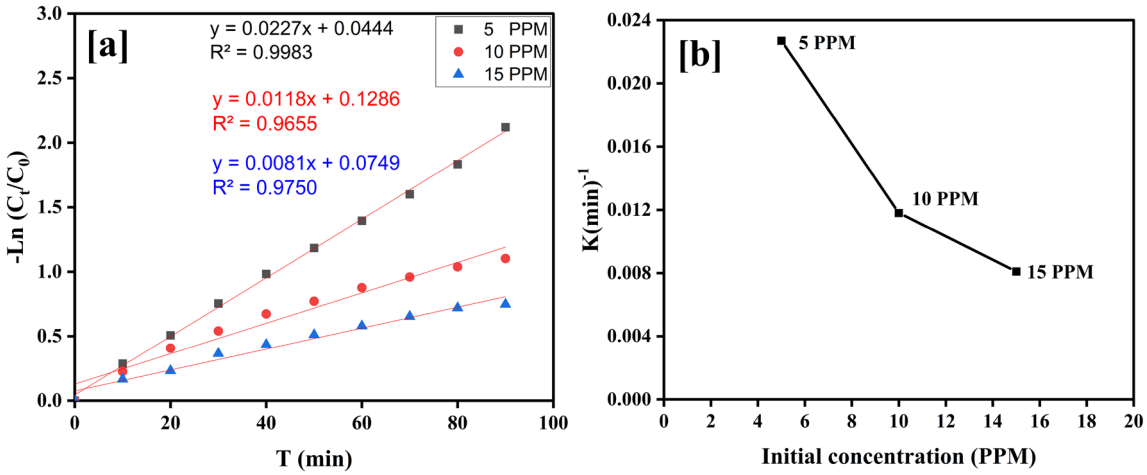

Fig. 16 **a** Pseudo-first-order reaction model for Basic fuchsine degradation under UV light irradiation and 10 mg nanocatalyst, 50 mL of 5, 10, and 15 ppm BF concentration, **b** The relation of apparent pseudo-first-order rate constants vs. initial concentration of BF

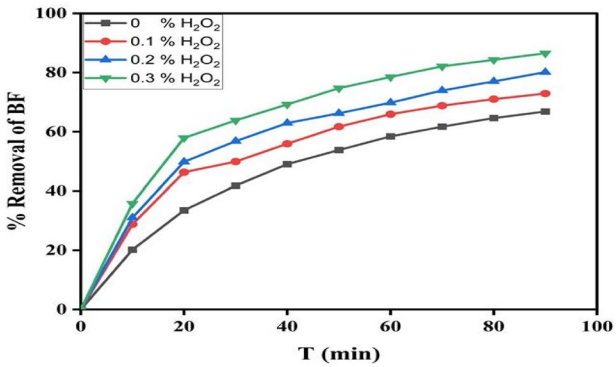

Fig. 17 % removal of Basic fuchsine by H_2O_2 (0, 0.1, 0.2 and 0.3%), Ag–TiO_2 (10 mg) and 50 mL of 10 ppm dye concentration under visible light irradiation

range into the visible spectrum [80]. Silver could introduce energy levels within the band gap, allowing the material to absorb visible light more efficiently. This enhanced light absorption ability enabled the effective utilization of solar energy for photocatalytic reactions [80]. Silver dopant could minimize the recombination of photo-induced charge carriers (electrons and holes); electrons generated by light absorption can transfer to the silver dopants, reducing the likelihood of recombination. Also, Silver dopant could induce oxygen vacancies that could act as trapping sites for charge carriers [81]. The potential mechanism can be described as follows [56, 82]. In the case of Ag–TiO_2 nanocomposites acting as photocatalysts, it has been observed that when exposed to visible light, there is a transfer of electrons from the highest occupied molecular orbital (HOMO) of oxygen (O) and titanium (Ti) atoms to the lowest unoccupied molecular orbital (LUMO) of silver (Ag). The highest occupied molecular orbital (HOMO) exhibits a pronounced affinity for an additional electron to restore its equilibrium state. In the process, a single electron is acquired from a water molecule, resulting in the formation of a hydroxyl radical (·OH). The active hydroxyl (OH) radicals function as a potent oxidizing agent, effectively breaking down BF molecules to generate the ultimate oxidation products. It is important to acknowledge that the mixing of Ag–TiO_2 nanocomposite with H_2O_2 has a synergistic impact, leading to the generation of (.OH) and HO_2^- radicals [56]. The cleavage of hydrogen peroxide (H_2O_2) catalysed by the silver-titanium dioxide (Ag–TiO_2) complex can be described by the following equations, which represent two essential processes:

$$\text{Ag-TiO}_2\text{NPs} + \text{H}_2\text{O}_2 \rightarrow^{+} \text{Ag-TiO}_2\text{NPs} + \text{HO}_2^{\cdot} + \text{H}^{+} \tag{2}$$

$$^{+}\text{Ag-TiO}_2\text{NPs} + \text{H}_2\text{O}_2 \rightarrow \text{Ag-TiO}_2\text{NPs} + {}^{\cdot}\text{OH} + \text{OH}^{-} \tag{3}$$

$$[1] + [2] : +2\text{H}_2\text{O}_2 \xrightarrow{\text{Ag–TiO}_2\text{ nanocatalyst}} {}^{\cdot}\text{OH} + \text{HO}_2^{\cdot} + \text{H}_2\text{O} \tag{4}$$

In addition to the photocatalytic activity exhibited by the Ag–TiO_2 nanocatalyst, the combined action of the Ag–TiO_2 nanocatalyst and H_2O_2 significantly enhances the overall photodegradation process by generating a greater number of active hydroxyl radicals (·OH). The potential photocatalytic mechanism is elucidated in Fig. 18.

In summary, Ag–TiO_2 anatase nanocomposites exposed exciting prospects as sustainable and efficient photocatalyst, with superior performance under visible light activation. Their tunable properties and enhanced performance inherit novel features for environmental remediation and energy conversion [83].

4 Conclusion

The aim of this work was to effectively synthesize a silver-doped anatase nanocomposite for wastewater treatment. The Ag–TiO_2 nanoparticles had the highest photocatalytic efficacy for BF, with a removal efficiency of 64% within a 90-min interval without H_2O_2. Furthermore, when combined with 0.3% H_2O_2 under visible light, the photocatalytic activity of the Ag–TiO_2 nanoparticles increased to 88%. The Ag–TiO_2 nanocomposite exhibits significant potential as a highly suitable option for the purpose of wastewater treatment. Our research offers a novel method for wastewater treatment by employing a promising nanoparticle. This strategy provides a cost-efficient solution to the urgent global water treatment issues.

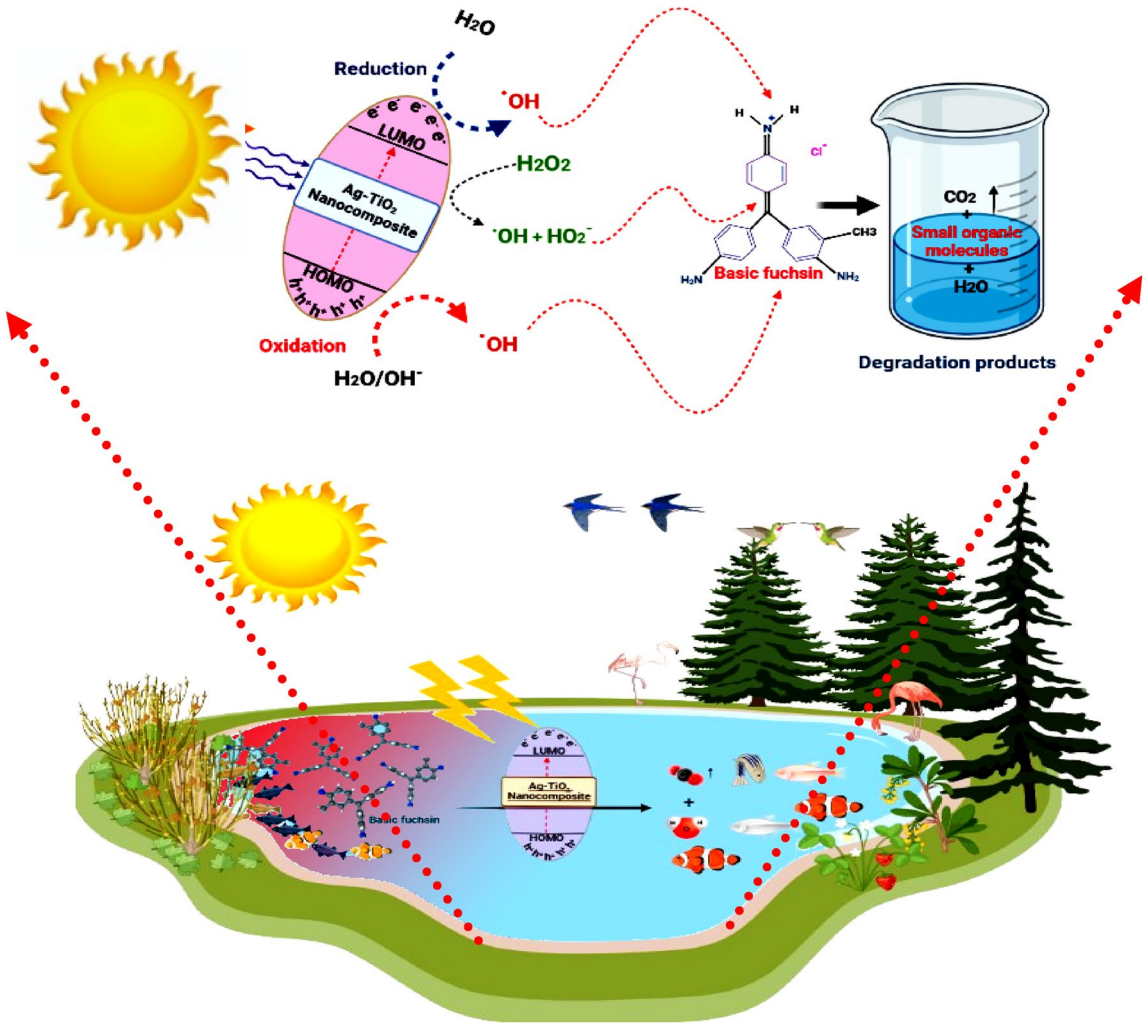

Fig. 18 The proposed photocatalytic mechanism of BF degradation by Ag–TiO_2 nanocatalyst in the presence of H_2O_2

Author contributions S.E.: Conceptualization, data curation formal analysis, and writing—original draft. A.M.E.: Conceptualization, data curation,formal analysis, and writing—original draft. M.A.E.: Formal analysis and writing—original draft. M.A.C.-D.: Writing—review—editing and supervision.

Funding Open access funding provided by The Science, Technology & Innovation Funding Authority (STDF) in cooperation with The Egyptian Knowledge Bank (EKB).

Availability of data and materials The data used to support the findings of this study are available from the corresponding author upon request.

Declarations

Competing interests The authors declare that they have no conflict of interest.

References

1. Shinde SK, et al. MOFs-graphene composites synthesis and application for electrochemical supercapacitor: a review. Polymers. 2022;14(3):511.
2. Mahmoudian MH, et al. Statistical modeling and optimization of dexamethasone adsorption from aqueous solution by Fe3O4@ NH2-MIL88B nanorods: Isotherm, kinetics, and thermodynamic. Environ Res. 2023;236:116773.
3. Norizan MN, et al. Heterojunctions of rGO/metal oxide nanocomposites as promising gas-sensing materials—a review. Nanomaterials. 2022;12(13):2278.
4. Naseri A, et al. Recent advances on dual-functional photocatalytic systems for combined removal of hazardous water pollutants and energy generation. Res Chem Intermed. 2022;48(3):911–33.
5. Nisar A, et al. Synthesis and characterization of ZnO decorated reduced graphene oxide (ZnO-rGO) and evaluation of its photocatalytic activity toward photodegradation of methylene blue. Environ Sci Pollut Res. 2022;29(1):418–30.
6. Azari A, et al. The superior adsorption capacity of 2, 4-Dinitrophenol under ultrasound-assisted magnetic adsorption system: Modeling and process optimization by central composite design. J Hazard Mater. 2021;418:126348.
7. Long Z, et al. Historical development and prospects of photocatalysts for pollutant removal in water. J Hazard Mater. 2020;395:122599.
8. Han S, et al. Plasma-assisted in-situ preparation of graphene-Ag nanofiltration membranes for efficient removal of heavy metal ions. J Hazard Mater. 2022;423:127012.
9. Elbasuney S, et al. Potential impact of reduced graphene oxide incorporated metal oxide nanocomposites as antimicrobial, and antibiofilm agents against pathogenic microbes: bacterial protein leakage reaction mechanism. J Clust Sci. 2022;34(2):1–18.
10. Paumo HK, et al. TiO2 assisted photocatalysts for degradation of emerging organic pollutants in water and wastewater. J Mol Liq. 2021;331:115458.
11. Rabiee F, et al. The superior decomposition of 2,4-dinitrophenol under ultrasound-assisted Fe3O4@TiO2 magnetic nanocomposite: process modeling and optimization, effect of various oxidants and degradation pathway studies. Int J Environ Anal Chem. 2022. https://doi.org/10.1080/03067319.2022.2034798.
12. Mhadhbi M, AbderazzakH, Avar B, Synthesis and properties of titanium dioxide nanoparticles. IntechOpen. 2023.
13. Hasanzadeh M, et al. Persulfate-assisted heterogeneous photocatalytic degradation of furfural from aqueous solutions using TiO2–ZnO/biochar composite. Heliyon. 2023;9(11):e21421.
14. Cha G, TiO 2 Nanotubes: a study of their optical and photocatalytic properties, and related applications. Friedrich-Alexander-Universitaet Erlangen-Nuernberg (Germany), 2021
15. Hashemi SY, et al. Degradation of Ceftriaxone from aquatic solution using a heterogeneous and reusable O3/UV/ Fe3O4@TiO2 systems: operational factors, kinetics and mineralisation. Int J Environ Anal Chem. 2022;102(18):6904–20.
16. Xu D, et al. Photocatalytic activity of Ag 2 MO 4 (M= Cr, Mo, W) photocatalysts. J Mater Chem A. 2015;3(40):20153–66.
17. Fan H, et al. Binary TiO2/RGO photocatalyst for enhanced degradation of phenol and its application in underground coal gasification wastewater treatment. Opt Mater. 2021;120:111482.
18. Makuła P, Pacia M, Macyk W. How to correctly determine the band gap energy of modified semiconductor photocatalysts based on UV–Vis spectra. J Phys Chem Lett. 2018;9(23):6814–7.
19. Wang Y, et al. A α-Fe2O3/rGO magnetic photocatalyst: enhanced photocatalytic performance regulated by magnetic field. J Alloys Compd. 2021;851:156733.
20. Xiong L, Tang J. Strategies and challenges on selectivity of photocatalytic oxidation of organic substances. Adv Energy Mater. 2021;11(8):2003216.
21. Ran J, et al. Earth-abundant cocatalysts for semiconductor-based photocatalytic water splitting. Chem Soc Rev. 2014;43(22):7787–812.
22. Lee KM, et al. Recent developments of zinc oxide based photocatalyst in water treatment technology: a review. Water Res. 2016;88:428–48.
23. Durmus Z, Kurt BZ, Durmus A. Synthesis and characterization of graphene oxide/zinc oxide (GO/ZnO) nanocomposite and its utilization for photocatalytic degradation of basic fuchsin dye. ChemistrySelect. 2019;4(1):271–8.
24. Zhang N, et al. Waltzing with the versatile platform of graphene to synthesize composite photocatalysts. Chem Rev. 2015;115(18):10307–77.
25. Qu Y, Duan X. Progress, challenge and perspective of heterogeneous photocatalysts. Chem Soc Rev. 2013;42(7):2568–80.
26. El-Khawaga AM, et al. Promising photocatalytic and antimicrobial activity of novel capsaicin coated cobalt ferrite nanocatalyst. Sci Rep. 2023;13(1):5353.
27. Yang J, et al. Roles of cocatalysts in photocatalysis and photoelectrocatalysis. Acc Chem Res. 2013;46(8):1900–9.
28. Kumbhakar P, et al. In-situ synthesis of rGO-ZnO nanocomposite for demonstration of sunlight driven enhanced photocatalytic and self-cleaning of organic dyes and tea stains of cotton fabrics. J Hazard Mater. 2018;360:193–203.
29. Sharma RK, et al. Silver nanomaterials: synthesis and (electro/photo) catalytic applications. Chem Soc Rev. 2021;50(20):11293–380.
30. Kavaliunas V, et al. Influence of Mg, Cu, and Ni dopants on amorphous TiO2 thin films photocatalytic activity. Materials. 2020;13(4):886.
31. Azari A, et al. Comprehensive systematic review and meta-analysis of dyes adsorption by carbon-based adsorbent materials: classification and analysis of last decade studies. Chemosphere. 2020;250:126238.
32. Azari A, et al. Magnetic NH2-MIL-101(Al)/Chitosan nanocomposite as a novel adsorbent for the removal of azithromycin: modeling and process optimization. Sci Rep. 2022;12(1):18990.
33. Abd Elkodous M, et al. Enhanced photocatalytic and antimicrobial performance of a multifunctional Cu-loaded nanocomposite under UV light: theoretical and experimental study. Nanoscale. 2018;10(4):1549–2172.
34. Fayoumi L, et al. Kinetic study of the degradation of crystal violet by K2S2O8. Comp Malachite Green. 2012;30(2):121–33.
35. Wang G, et al. Structural study of titanium oxide films synthesized by ion beam-assisted deposition. Scan J Scan Microsc. 2008;30(2):59–64.
36. Qu H-J, et al. A review of graphene-oxide/metal–organic framework composites materials: characteristics, preparation and applications. J Porous Mater. 2021;28(6):1837–65.
37. Rezaei A, et al. Magnetic and photo-catalyst BaFe12O19-ZnO: Hydrothermal preparation of barium ferrite nanoparticles and hexagonal zinc oxide nanostructures. J Mater Sci: Mater Electron. 2017;28(9):6607–18.

38. Rahmanifar MS, et al. A dual Ni/Co-MOF-reduced graphene oxide nanocomposite as a high performance supercapacitor electrode material. Electrochim Acta. 2018;275:76–86.
39. Zango ZU, et al. A critical review on metal-organic frameworks and their composites as advanced materials for adsorption and photocatalytic degradation of emerging organic pollutants from wastewater. Polymers. 2020;12(11):2648.
40. Rahman KH, Kar AK, Chen K-C. *Oxidation-induced catalytic performance of heterostructured* Ni–TiO_2 *nanoparticles and formation of Leuco-Methylene blue*. Res Chem Intermed. 2022;48(11):4475–501.
41. Li Q, et al. Disclosing support-size-dependent effect on ambient light-driven photothermal CO2 hydrogenation over nickel/titanium dioxide. Angewandte Chem. 2024;136(10):e202318166.
42. Shahid K, et al. Northumbria research link. IEEE Trans Neural Syst Rehabil Eng. 2022;30:8–19.
43. Bumajdad A, Madkour M. Understanding the superior photocatalytic activity of noble metals modified titania under UV and visible light irradiation. Phys Chem Chem Phys. 2014;16(16):7146–58.
44. Tantawy HR, et al. Novel synthesis of bimetallic Ag-Cu nanocatalysts for rapid oxidative and reductive degradation of anionic and cationic dyes. Appl Surf Sci Adv. 2021;3:100056.
45. Patel KJA. Flow injection determination of anionic surfactants with cationic dyes in water bodies of central India. Analyst. 1998;123(8):1691–5.
46. Xu J, et al. Synthesis and optical properties of silver nanoparticles stabilized by gemini surfactant. Coll Surf A: Physicochem Eng Asp. 2006;273(1–3):179–83.
47. Vineh MB, et al. Biodegradation of phenol and dyes with horseradish peroxidase covalently immobilized on functionalized RGO-SiO2 nanocomposite. Int J Biol Macromol. 2020;164:4403–14.
48. Dawam M, et al. Regeneration of phenol exhausted activated carbons used in the operations of water treatment by domestic microwave Oven. Int J Sci Res Chem Sci. 2021;8(2):11–7.
49. Abd Elkodous M, et al. Carbon-dot-loaded CoxNi1−xFe2O4; x= 09/SiO2/TiO2 nanocomposite with enhanced photocatalytic and antimicrobial potential: an engineered nanocomposite for wastewater treatment. Sci Rep. 2020;10(1):1–22.
50. Seery MK, et al. Silver doped titanium dioxide nanomaterials for enhanced visible light photocatalysis. J Photochem Photobiol A: Chem. 2007;189(2–3):258–63.
51. Van Tran T, et al. Central composite design for optimizing the organic dyes remediation utilizing novel graphene oxide@ CoFe2O4 nanocomposite. Surf Interfaces. 2020;21:100687.
52. Ruidíaz-Martínez M, et al. Hydrothermal synthesis of rGO-TiO2 composites as high-performance UV photocatalysts for ethylparaben degradation. Catalysts. 2020;10(5):520.
53. El-Khawaga AM, et al. Antimicrobial and photocatalytic degradation activities of chitosan-coated magnetite nanocomposite. J Cluster Sci. 2021;32(5):1107–19.
54. Elbasuney S, et al. Enhanced photocatalytic and antibacterial activities of novel Ag-HA bioceramic nanocatalyst for waste-water treatment. Sci Rep. 2023;13(1):13819.
55. Bora LV, Mewada RKJR, Reviews SE. Visible/solar light active photocatalysts for organic effluent treatment: fundamentals, mechanisms and parametric review. Renew Sustain Energy Rev. 2017;76:1393–421.
56. Wang D, et al. Photocatalytic degradation of organic dye and phytohormone by a Cu (II) complex powder catalyst with added H2O2. Coll Surf A: Physicochem Eng Asp. 2020;603:125147.
57. Abd Elkodous M, et al. Cocatalyst loaded Al-SrTiO3 cubes for Congo red dye photo-degradation under wide range of light. Sci Rep. 2023;13(1): 6331.
58. Ollis DF. Kinetics of photocatalyzed reactions: five lessons learned. Front Chem. 2018;6:378.
59. Na-Phattalung S, et al. Band gap narrowing of TiO2 nanoparticles: A passivated Co-doping approach for enhanced photocatalytic activity. J Phys Chem Solids. 2022;162:110503.
60. Divya G, et al. Improved catalytic efficiency by N-doped TiO2 via sol gel under microwave irradiation: dual applications in degradation of dye and microbes. Hybrid Adv. 2022;1:100010.
61. Chakhtouna H, et al. Recent progress on Ag/TiO2 photocatalysts: photocatalytic and bactericidal behaviors. Environ Sci Pollut Res. 2021;28(33):44638–66.
62. Mahmoodi NMJD. Photocatalytic ozonation of dyes using copper ferrite nanoparticle prepared by co-precipitation method. Desalination. 2011;279(1–3):332–7.
63. Ellouzi I, et al. Glucose-assisted ball milling preparation of silver-doped biphasic TiO2 for efficient photodegradation of Rhodamine B: effect of silver-dopant loading. Chem Phys Lett. 2021;770:138456.
64. Kong Y, et al. Synergistic silver doping and N vacancy promoting photocatalytic performances of carbon nitride for pollutant oxidation and hydrogen production. Chem Eng J. 2024;479:147676.
65. Cozzoli PD, et al. Photocatalytic activity of organic-capped anatase TiO2 nanocrystals in homogeneous organic solutions. Mater Sci Eng, C. 2003;23(6):707–13.
66. Groeneveld I, et al. Parameters that affect the photodegradation of dyes and pigments in solution and on substrate—an overview. Dyes Pigm. 2023;210:110999.
67. Ola O, Maroto-Valer MM. Review of material design and reactor engineering on TiO2 photocatalysis for CO2 reduction. J Photochem Photobiol, C. 2015;24:16–42.
68. Seery MK, et al. Silver doped titanium dioxide nanomaterials for enhanced visible light photocatalysis. J Photochem Photobiol, A. 2007;189(2):258–63.
69. Wang T, et al. Plasmonic photocatalysis: mechanism, applications and perspectives. Chin J Struct Chem. 2023;42(9):100066.
70. Tahir M, Amin NS. Indium-doped TiO2 nanoparticles for photocatalytic CO_2 reduction with H_2O vapors to CH_4. Appl Catal B. 2015;162:98–109.
71. Abdoallahzadeh H, et al. Application of green and red local soils as a catalyst for catalytic ozonation of fulvic acid: experimental parameters and kinetic. Biomass Convers Biorefin. 2023. https://doi.org/10.1007/s13399-023-03895-6.

72. Hashemi SY, et al. Application of Response Surface Methodology (RSM) in optimisation of fluoride removal by magnetic chitosan/graphene oxide composite: kinetics and isotherm study. Int J Environ Anal Chem. 2023;103(17):5368–86.
73. El-Khawaga AM, et al. Synthesis and applicability of reduced graphene oxide/porphyrin nanocomposite as photocatalyst for waste water treatment and medical applications. Sci Rep. 2022;12(1):17075.
74. Wahab HS, Hussain AA. Photocatalytic oxidation of phenol red onto nanocrystalline TiO2 particles. J Nanostr Chem. 2016;6(3):261–74.
75. Taamallah A, Merouani S, Hamdaoui O. Sonochemical degradation of basic fuchsin in water. Desalin Water Treat. 2016;57(56):27314–30.
76. Goodarzi N, et al. Recent progress on semiconductor heterogeneous photocatalysts in clean energy production and environmental remediation. Catalysts. 2023;13(7):1102.
77. Lu S, et al. Recent advances in novel materials for photocatalytic carbon dioxide reduction. Carbon Neutr. 2024;3(1):142–68.
78. Rauf MA, Meetani MA, Hisaindee S. An overview on the photocatalytic degradation of azo dyes in the presence of TiO2 doped with selective transition metals. Desalination. 2011;276(1–3):13–27.
79. Armaković SJ, Savanović MM, Armaković S. Titanium dioxide as the most used photocatalyst for water purification: an overview. Catalysts. 2023;13(1):26.
80. Khan M, et al. Effect of Ag doping concentration on the electronic and optical properties of anatase TiO2: a DFT-based theoretical study. Res Chem Intermed. 2013;39(4):1633–44.
81. Etacheri V, et al. Visible-light activation of TiO2 photocatalysts: advances in theory and experiments. J Photochem Photobiol, C. 2015;25:1–29.
82. Harikishore M, et al. Effect of Ag doping on antibacterial and photocatalytic activity of nanocrystalline TiO2. Proc Mater Sci. 2014;6:557–66.
83. Wen Y, Ding H, Shan Y. Preparation and visible light photocatalytic activity of Ag/TiO2/graphene nanocomposite. Nanoscale. 2011;3(10):4411–7.